University of Crete
Physics Department

MEASURING OPTICAL POLARIZATION IN LOW DUST EXTINCTION REGIONS

Raphael Skalidis

Master Thesis
supervised by prof. K. Tassis

January 2018

Acknowledgements

I would like to express the deepest appreciation to my supervisor K. Tassis, who continually and convincingly conveyed a spirit of creativity in regard to the work. Many thanks to G.V.Panopoulou and V. Pavlidou for their comments and discussions on various topics of this work. I thank I. Komis for his contribution during the first step of this work. Moreover, I would like to thank D. Blinov, K. Kovlakas, T. Kougentakis, N. Mandarakas and G. Paterakis for technical support. Finally, I would like to express my gratitude to Dr K. Xristidis for fruitful discussions and his constant moral support. This thesis makes use of VOSA, developed under the Spanish Virtual Observatory project supported from the Spanish MICINN through grant AyA2011-24052.

Abstract

Galactic dust polarized emission contaminates the signal of cosmic microwave background (CMB) which is assumed to bare a B-mode polarization pattern caused during the inflationary epoch. PASHIPAE is an experiment which aspires to treat dust contamination by delivering optical polarization data for millions of stars at regions where observations of CMB are being performed (high galactic regions, $|b| > 50^{\circ}$). In this work we did a mini pathfinder polarization survey for PASHIPAE in order to investigate what is the lowest detectable optical polarization in the sky. We observed regions with minimum dust extinction and found that measuring polarization with an accuracy 0.1% PASHIPAE will be able to deliver polarization measurements for the whole sky except a small part which in total is 20.3 square degrees.

Contents

Chapter 1

INTRODUCTION

A diffuse radiation known as *cosmic microwave background (CMB)* exists in the universe. It is a residual left over from an early stage of the Big Bang. This radiation is assumed to be polarized. The polarization bares a characteristic feature of a B-mode pattern due to gravitational wave interaction during the inflationary epoch ([Seljak(1997)], [Seljak & Zaldarriaga(1997)], [Kamionkowski et al.(1997)I], [Zaldarriaga & Seljak(1997)], [Kamionkowski et al.(1997)II]); or induced by gravitational lensing caused by density inhomogeneities ([Zaldarriaga & Seljak(1998)]). The detection of the B-mode pattern would provide strong evidence of the inflation epoch and by extension of quantum gravity. Without exaggeration the B-mode polarization feature is the 'holy grail' of modern physics and this is why many of experiments are competing for its detection. Some of these are BICEP3, AdvACT, CMB-S4, PIPER, LiteBIRD, PRISM, COrE+, PIXIE, POLARBEAR-2 ([Inoue et al.(2016)]).

In 2014 [BICEP2] team announced the detection of a B-mode signal. However, follow up studies ascribed this detection to the contamination by the polarized emission of galactic dust [Planck Col.(2016)]. Galactic dust is ubiquitous in the Galaxy and operates as a veil which in addition emits diffuse black body radiation at far-IR and absorbs starlight passing through it. Both dust emission and starlight absorption are polarized at far-IR and at optical wavelengths respectively because of the interaction between galactic dust and magnetic field. Asymmetric dust grains tend to orient their short axis with the magnetic field lines ([Hiltner(1949)II], [Andersson et al.(2015)]) and as a result their thermal emission is polarized perpendicular to this axis ([Cudlip et al.(1982)], [Stein(1966)]) at far-IR. On the other hand, starlight which passes through a dusty region is preferentially absorbed across the long axis of dust grains; this results in the starlight becoming polarized parallel to the field lines ([Cudlip et al.(1982)], [Stein(1966)]). Thus, the magnetic field can be traced through the polarization caused by dust ([Davis(1951)], [Chandrasekhar & Fermi(1953)]). Cartoon in Figure 1.1 [Tassis(2014)] shows graphically the whole process.

A common way to treat the contamination problem caused by polarized dust emission is to extrapolate the signal from frequencies were dust dominates ($\sim$ 350 GHz) to frequencies where the experiment is being performed ($\sim$ 60-150 GHZ in the case of [BICEP2]). However, the extrapolation between different frequencies of the polarized

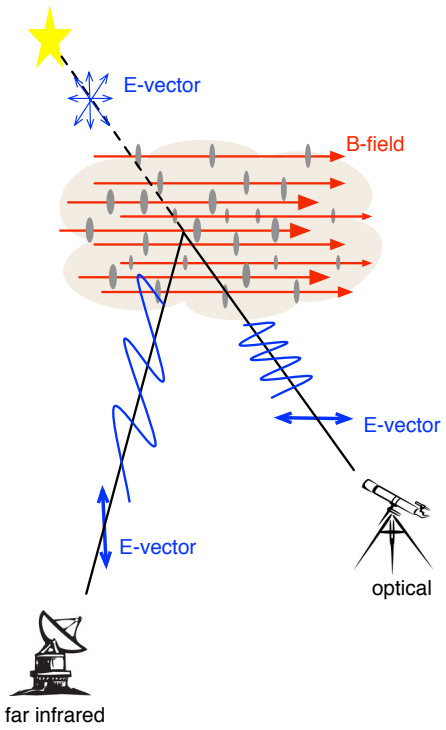

Figure 1.1: Asymmetric dust grains align their short axis parallel to the magnetic field lines. Red lines show the direction of the magnetic field (B-field). Initially unpolarized starlight is detected linearly polarized along the B-field when it passes through a cloud which contains asymmetric dust grains. The black body dust emission is polarized perpendicular to the B-field.

dust emission may become inaccurate. It has been shown that two interstellar clouds, under certain conditions, when they interfere across the same line-of-sight are adequate to decorrelate polarization between the frequency maps [Tassis & Pavlidou(2015)]; hence the extrapolation can mimic the B-mode signal and lead to erroneous conclusions about the existence of gravitational primordial waves. The conditions for this decorrelation to be significant are: 1) the magnetic fields between the clouds are misaligned and 2) the ratio of the polarized intensities between the two clouds changes between the frequencies of extrapolation.

Almost in all lines-of-sight two or more clouds exist, even at high Galactic latitudes. Thus, CMB B-mode experiments have to consider this effect. Knowledge of the direction of the magnetic field of both clouds and the ratio between the polarized intensities between the two clouds is necessary. Information along the line of sight of the magnetic field is needed too. Thermal emission cannot provide this information because its intensity is the result of integration along the line-of-sight to infinity, hence distance information is lost. Optical polarization, on the other hand, depends on each star's

distance.

The majority of the stellar optical polarization observations, however, have been driven by the star formation community hitherto, hence they are agglomerated near the galactic plane ([Clemens et al.(2012)]; [Heiles(2000)]); on the other hand, CMB experiments target regions high above the galactic plane in order to avoid contamination from dust. Thus, optical polarization data lack at regions where CMB experiments target (high galactic latitude regions). This is the scope of PASHIPAE project; to make a complete optical polarization mapping towards the galactic poles.

Optical polarization, at these regions is yet unexplored. There have been some high galactic latitude surveys ([Berdyugin et al.(2001)I], [Berdyugin et al.(2011)II]), but they accounted only for the brightest stars and for stars with known distances. This biases their sample and makes it unrepresentative of the polarization governing the low dust content regions of the interstellar medium. The scope of this work is to explore low dust content regions in a more systematic way by using a photometrically complete sample of stars.

Moreover, our survey sheds light on the relation of polarization, p, as a function of dust extinction, A_v, at the low extinction regime. Polarization is correlated with dust extinction, hence with dust column density. Fig. 1.2 ([Andersson & Potter(2005)], [Klare et al.(1972)]) shows polarization as a function of dust total extinction. The black solid line sets the upper envelope between the two quantities. The bound is described by the relation:

$$\frac{p}{A_v} \approx 3\% \tag{1.1}$$

Few polarization data exist at low extinction, below $A_v \sim 0.3$ mag. With our mini polarization survey we deliver polarization values at this low A_v regime.

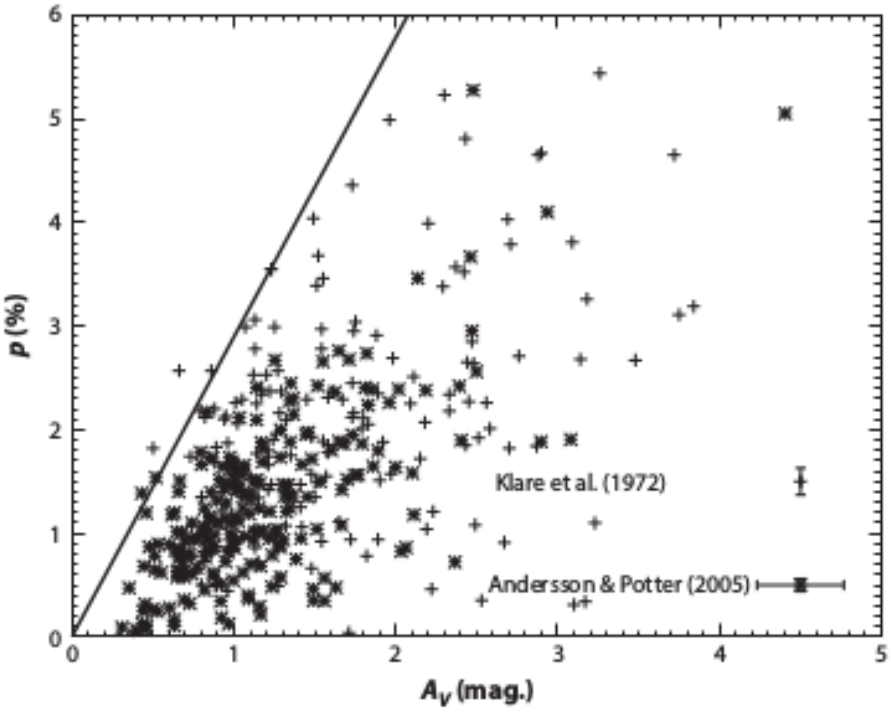

Figure 1.2: Polarization, p, as a function of extinction A_v. Relation 1.1 is indicated by the solid line. Polarization data at both optical and near-IR are included in this plot [Andersson et al.(2015)].

Chapter 2

OBSERVATIONS

As a pathfinder towards PASHIPAE, we conducted three small-scale surveys in regions of the high latitude sky where the dust column is low. Fig. 2.1 marks the centers of the regions with black circles in the Planck 353 GHz thermal dust emission map [Planck Col.(2013)]. Regions with black color correspond to high dust emission regions, while regions covered with white color correspond to lower dust emission. Fig. 2.2 marks the centers of the regions with red stars in the Lenz map [Lenz et al.(2017)]. The colored lines in the map mark the regions where different CMB experiments are being performed. The three regions were selected within the PASHIPAE footprint ($|b| > 50°$), according to visibility constraints. Fig. 2.3 shows the distribution of E(B-V) magnitudes in the galactic map (constructed by [Lenz et al.(2017)]). The blue histogram is the E(B-V) distribution for the whole map and the green for regions at $|b| > 50°$. The mean extinction of each of the three regions we targeted is shown with the vertical lines. For the remainder of the paper, we refer to these regions as *dark patches (dps)* (because of their low dust emission in the Planck map). We refer to the region with lowest extinction as *dark patch 1 (dp1)*, that with middle extinction *dark patch 2 (dp2)* and that with higher extinction as *dark patch 3 (dp3)*. For dp1 (solid line) the E(B-V) value is 0.0063 mag, for dp2 (dotted line) is 0.0072 mag and for dp3 (dash dotted line) is 0.0118 mag. In Lenz map 20.3, 66.8 and 1296.6 square degrees in total correspond to high latitude regions ($|b| > 50°$) with E(B-V) values lower than that one of dp1, dp2 and dp3 respectively. The three regions dp1, dp2, dp3 are centered at l, b = [124.7, 60.0], l, b = [159.4, 49.0] and l, b = [191.1, 48.6] respectively.

Observations were conducted in the *R*-band using the RoboPol optical polarimeter. RoboPol is a 4-channel imaging polarimeter mounted on the 1.3.-m telescope at Skinakas Observatory in Crete, Greece[1]. The instrument is designed to measure Stokes parameters I, q and u simultaneously by splitting every light ray detected into a vertical and a horizontal component. As a result each point in the sky is projected to four points in the CCD camera. The instrument field of view (FOV) is 13'×13' wide. The central part of the FOV (4'×4') is shadowed by a focal plane mask whose purpose is to lower the background for targets that are placed in the center of the FOV. For this project,

[1] http://skinakas.physics.uoc.gr/

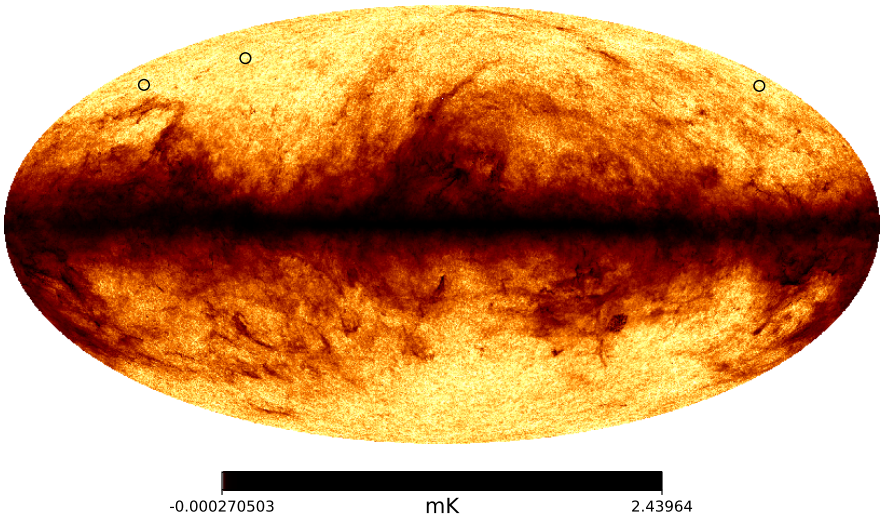

Figure 2.1: All sky map of the dust intensity at 353 GHz. The black circles mark the three regions targeted with RoboPol.

the required precision can only be obtained by pointing targets in the mask. For more details on the instrument's operation see [King et al.(2014)].

The size of the regions was selected to be comparable to the field of view of our instrument: $15' \times 15'$. Within these areas we constructed flux-limited samples. Stars with $12 < R_{mag} < 16.5$ were selected from the USNOB catalog. We discarded stars that would suffer from confusion from nearby sources. Due to observing time limitations our final samples are complete down to 16.47 for dp1, 15.7 for dp2 and down to 16.25 for dp3 (with an additional star of 16.6 mag).

Observations took place in the period, May-August 2015 for dp1, September-November 2015 for dp3 and October-November 2017 for dp2. The observing time was 27.5 hours for dp1, 16 hours for dp2 and 20 hours for dp3. In summary we observed 68 stars from which 24 were in dp1, 23 in dp2 and 21 in dp3. During each night of observation eight polarization standards, which are used for calibration purposes, were observed.

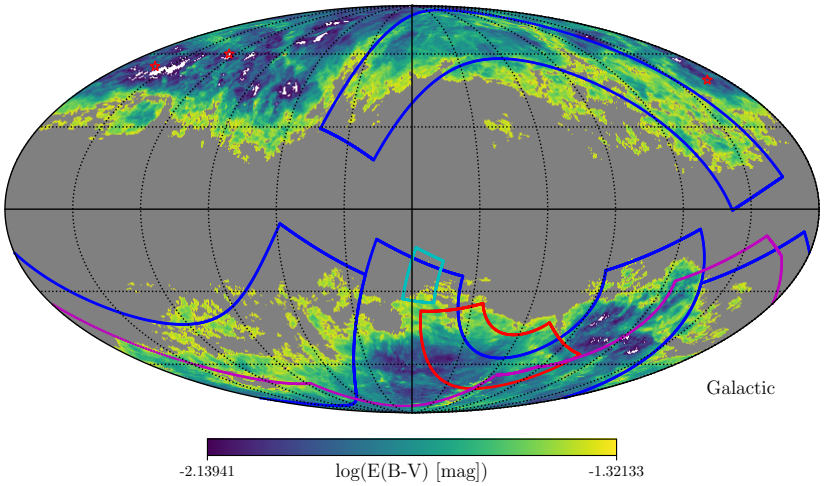

Figure 2.2: All sky map of the E(B-V) derived from HI emission [Lenz et al.(2017)]. The red stars mark the regions targeted. The regions with dp1 < E(B-V) < dp2 are shown in white. Regions with E(B-V) < dp1 are shown in dark gray. Lines mark the target regions of the following CMB polarization experiments: AdvACT (blue), [BICEP2] (red), [EBEX] (cyan), [SPIDER] (magenta)

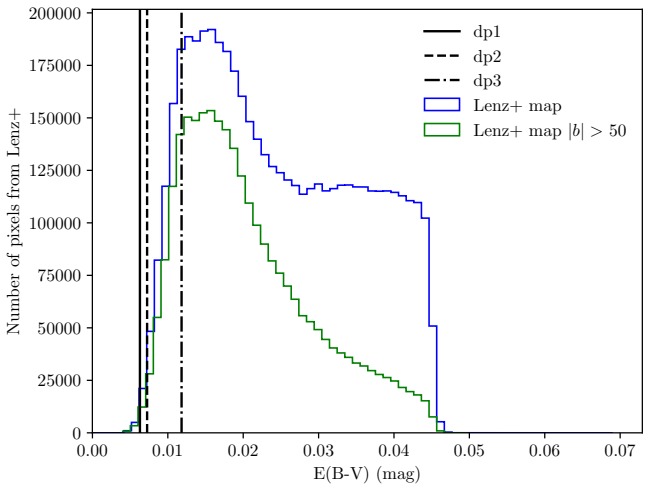

Figure 2.3: Distribution of pixel intensities from the E(B-V) map of [Lenz et al.(2017)]. Blue histogram corresponds to whole map pixel's distribution. The green distribution is the distribution of pixel's located at $|b| > 50$. Vertical lines correspond to dp1, dp2 and dp3 mean extinction values.

Chapter 3

DATA REDUCTION

The data were reduced using the RoboPol pipeline [King et al.(2014)]. We explain the basic steps here. We use the latest version of the pipeline which includes some modifications [Panopoulou et al.(2016)].

3.1 RoboPol pipeline

Linear polarization, p, and its electric vector position angle (EVPA or χ) can be written in terms of relative Stokes parameters as:

$$p = \sqrt{q^2 + u^2}, \quad \sigma_p = \sqrt{\frac{q^2\sigma_q^2 + u^2\sigma_u^2}{q^2 + u^2}} \tag{3.1}$$

$$\chi = \frac{1}{2}\arctan(\frac{u}{q}), \quad \sigma_\chi = \frac{1}{2}\sqrt{\frac{u^2\sigma_q^2 + q^2\sigma_u^2}{(q^2 + u^2)^2}} \tag{3.2}$$

RoboPol projects each point in the sky into four spots and measures Stokes parameters I, q, u simultaneously. Fig.3.1 illustrates a star as is observed in the mask of RoboPol. The expression which gives the relative Stokes parameters and the uncertainties are:

$$\begin{aligned} q &= \frac{N_1 - N_0}{N_1 + N_0}, \quad \sigma_q = \sqrt{\frac{4(N_1^2\sigma_0^2 + N_0^2\sigma_1^2)}{(N_0 + N_1)^4}} \\ u &= \frac{N_2 - N_3}{N_2 + N_3}, \quad \sigma_u = \sqrt{\frac{4(N_3^2\sigma_2^2 + N_2^2\sigma_3^2)}{(N_2 + N_3)^4}} \end{aligned} \tag{3.3}$$

where $N_0, .., N_4$ are the intensities of the four spots and $\sigma_0, .., \sigma_4$ the uncertainties in the intensities respectively.

3.1.1 The qu plane

In linear polarization it is easier to measure q and u. However, because the physical quantities are the degree of polarization and the polarization direction we transform q

and u to p and χ using equations 3.1 and 3.2. For this reason it is common to present the observations in the qu plane.

Each q, u measurement corresponds to a point in the qu plane. The distance from the origin of each point is the polarization amplitude, p, of this measurement. The angle, θ, between q and u in the qu plane is:

$$\theta = \arctan(\frac{u}{q}) \tag{3.4}$$

If we compare θ and χ (equation 3.2) we get the relation $\theta = 2\chi$. Angle θ is defined in the range $[0, 2\pi]$, hence χ is defined in the range $[0, \pi]$. In this work all the measurements are presented in the qu plane.

3.2 Aperture photometry

Each spot's intensity $N_i (i = 1, 2, 3, 4)$ is computed by using circular apertures centered on the center of each spot (red circles in Fig.3.1). However, this measurement is contaminated by background sources (e.g sky brightness). In order to eliminate it we measure background's intensity level in a region bounded by two outer annuli (green and blue circles in Fig.3.1) and subtract this value from the spot's measured intensity. Because the focal plane mask restricts the area around the spot where we can measure background's intensity a squared region is used to maximize the pixels used in the computation (blue boxes in Fig.3.1).

Systematic uncertainties or bad seeing or bad weather conditions during the observations can cause the point spread functions of each spot to be distorted in different ways. It has been noticed that spots of the same direction are distorted in the same way so we use the same aperture for vertical spots and a different aperture for horizontal spots. Both apertures have been selected so they are optimized in containing all the light while retaining the smallest distance from the source. In order to find it we measure the intensity for each spot for various apertures; as the aperture increases the intensity of the spot increases until a critical aperture above which the source contains no more light, hence the intensity remains almost constant. This critical aperture is optimized for photometry purposes. Fig.3.2 illustrates, the intensity versus aperture (as a multiple of the full width at half maximum FWHM) curves , for each of the four spots of an observed target. Vertical lines show the optimized apertures. In order to locate the optimized aperture in practice we solve the equation:

$$\frac{dP}{dx} = \lambda P(x) \tag{3.5}$$

In order to compute λ we processed many standard stars and we selected the value that yields the most accurate optimal apertures: $\lambda = 0.01$.

3.3 Instrument's calibration

Due to systematic errors of the instrument's mask we have to calibrate the observations. For this reason, for each night of observation, we observed some standard stars which

Table 3.1: Polarization standard stars used for calibration.

	P(%)	$\chi(\circ)$	Band	References
BD+32.3739	0.025±0.017	35.79°	V	1
BD+33.2642	0.231±0.031	12.67°	V	1
BD+59.389	6.430±0.022	98.14° ± 0.10°	R	1
HD183143	5.700 ± 0.040	178.0° ± 1.00°	R	3
HD212311	0.034 ± 0.021	50.99°	V	1, 4
	0.020 ± 0.021	36.2°± 25.3 °		
HD14069	0.022 ± 0.019	156.57°	V	1
G191B2B	0.061 ± 0.038	147.65°	V	2

(1) [Schmidt et al.(1992)], (2)[Rautela et al.(2004)], (3)[Hsu & Breger(1982)], (4)[Eswaraiah et al.(2011)]

Table 3.2: Instrument's systematic errors in q, u.

	$q_{obs} - q_{standard}(\%)$	$u_{obs} - u_{standard}(\%)$
dp1	0.023± 0.111	-0.350 ± 0.0100
dp2	0.171± 0.105	-0.293± 0.113
dp3	0.008± 0.001	-0.368± 0.066

are stable and have a well defined polarization value in the literature (Table3.1). The observed values are subtracted from the literature ones and the residual indicates what is the instrument's systematic error.

Fig. 3.3 plots the q_{obs}, u_{obs} measurements of standard stars subtracted from their literature values $q_{standard}$, $u_{standard}$. Measurements for dp1 standards are illustrated in the top panel, in the middle panel for dp2 and in the bottom for dp3. The deviation from zero declares that the instrument intrinsically shifts all the observations towards more positive q and more negative u values. In table 3.2 we present the centroid of q and u error for each region.

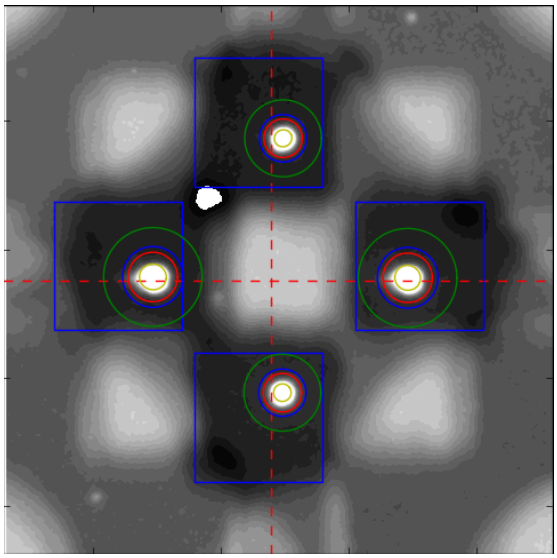

Figure 3.1: A star observed with RoboPol's focal plane mask. The spots are enumerated as follows: 0 is the up spot, 1 is the down, 2 is the right and 3 is the left spot. The red circle illustrates the circular region used for photometry. The blue and green mark the region where the background's intensity is computed, while the yellow circles are the Cron-apertures (we do not use them in this work). The blue box marks the region which is used to maximize the pixels used in the background's intensity estimation. The red dashed lines locate mask's geometrical center.

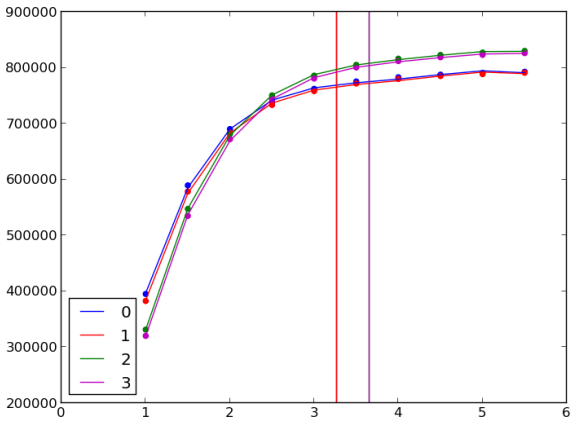

Figure 3.2: An example of background subtracted counts versus aperture (measured as multiples of FWHM) for each of the four spots. The bottom left legend shows which color corresponds to which spot. Vertical lines mark the optimized apertures found by the polynomial fit.

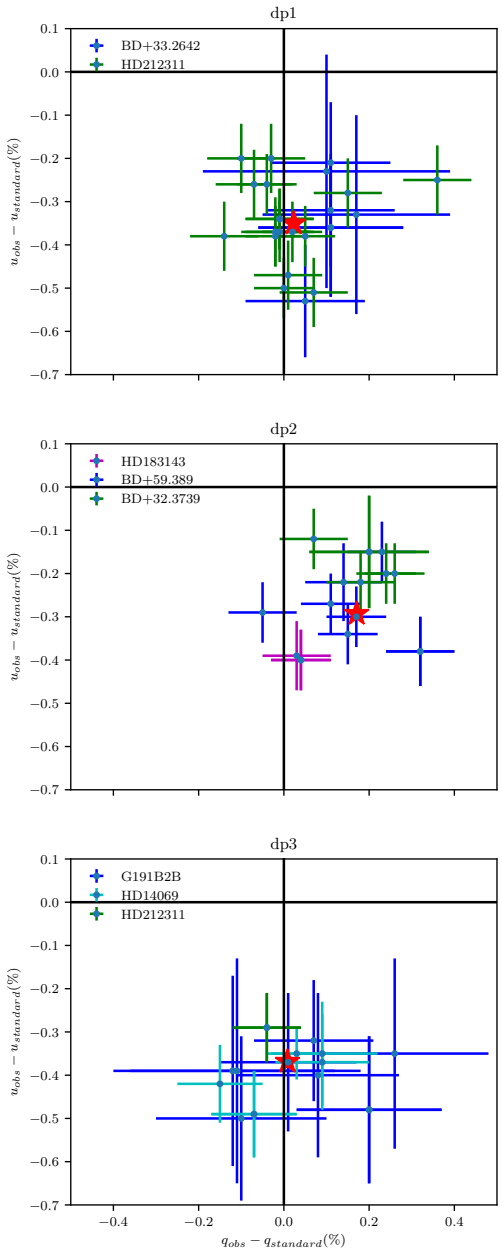

Figure 3.3: The q_{obs}, u_{obs} observations of standard stars subtracted from their literature values $q_{standard}, u_{standard}$. The red star illustrated in each case is the centroid of the measurements. All values are presented in percentages.

Chapter 4

DATA RESULTS

4.1 Polarization measurements

4.1.1 Measurements on the qu plane

Applying the data reduction of RoboPol pipeline, as described in the previous chapter and correcting for instrumental systematic errors, we obtain the polarization measurements shown in Fig. 4.1. The red star which appears in each dp corresponds to the weighted mean of q and u measurements.

Inspecting the results in qu plane in Fig. 4.1 we notice that most of the measurements in each dp are agglomerated near zero. This is an expected result for regions with so low dust content. However, some significant detections appear with signal-to-noise-ratio (SNR) higher than 3. This mostly happens for fainter stars.

Starting with dp3, the tendency of q, u measurements towards the first quadrant indicates the existence of a dominant cloud. Starlight polarization follows the direction of magnetic field of the cloud and as a consequence q and u measurements present anisotropies towards certain directions. Fig. 4.4 plots the HI spectra taken along the line-of-sight of the mean RA and DEC of each region. The green spectrum is for dp3 and it shows two prominent peaks. The location of the majority of the measurements on the qu plane in the first quadrant can be explained by the contribution of these two clouds.

In dp2 (middle panel in Fig. 4.1) appears a slight anisotropy towards the first and fourth quadrant. There are some highly polarized stars in the fourth quadrant except of a single measurement which is located in the second quadrant. The location of q and u measurements is not so anisotropic as in dp3 but still a slight preference can be distinguished towards the right quadrants of the qu plane. Looking at the HI spectrum of dp2 in Fig.4.4 orange line a low intensity HI cloud exists. The weak HI intensity in this region may explain the low anisotropy of q, u measurements in dp2.

The last and most complicated case is dp1. It is the region with the lowest extinction, however, in the qu plane (left panel Fig. 4.1) there are some highly polarized outlying stars. The suspicious thing with this outliers is that they are sparsely located in the qu plane and they do not show a preferred direction as the existence of an interstellar cloud

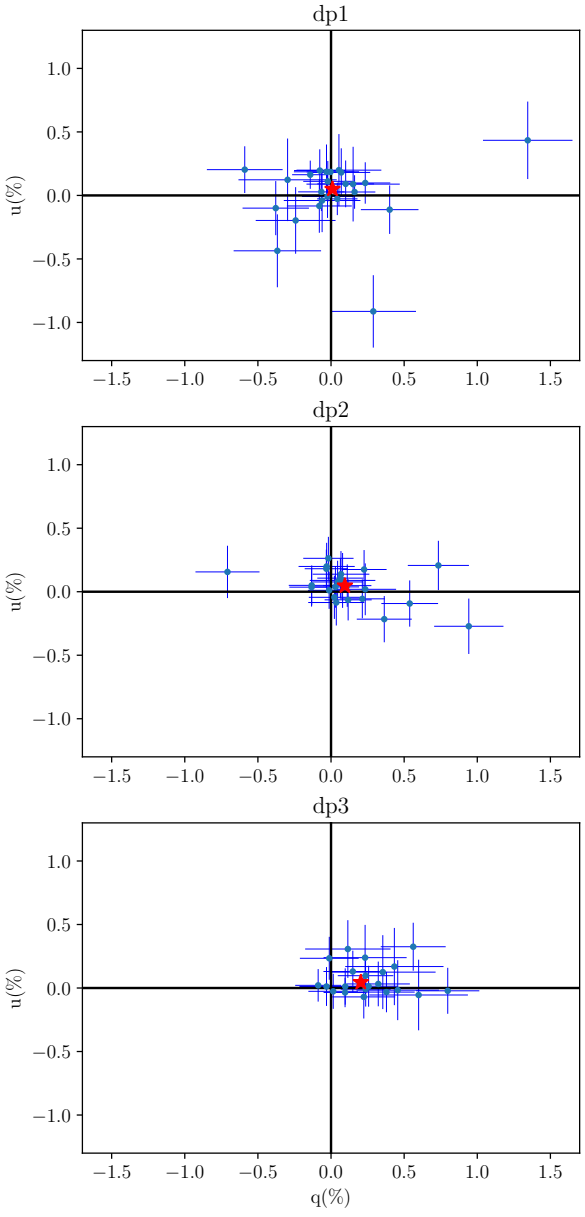

Figure 4.1: The *qu* plane derived for each region after instrument's error correction. The red star in each panel corresponds to the weighted mean of q and u measurements ($q_{averaged}$, $u_{averaged}$ in table 4.1).

would imply. Moreover, most of the measurements are well centered at zero. In general the location of measurements of this region is more symmetric than the other cases and seems consistent with a non-polarized region. However, the HI data spectrum of dp1, Fig.4.4 the blue line, reveals two low intensity clouds. If we consider that cloud of dp2 can barely induse a slight anisotropy in qu plane we conclude that clouds of dp1 are inadequate to cause any. This is why dp1 measurements are symmetrically distributed.

Outlying qu measurements

For all of the outlying stars in dp1 and dp2 we investigated the possibility to be quasar candidates, which are intrinsically polarized. Quasars deviate from the black body spectrum. In order to investigate whether the outlying sources are black bodies we used VOSA [Bayo et al.(2008)]. VOSA is a tool which uses historical multi-band photometric data in order to construct the spectral energy distribution of a source. We fitted the simplest stellar spectra model of VOSA to the outlying targets and they are consistent with the black body spectrum. Moreover, we computed their effective temperatures. If the source temperature is lower than a typical star temperature, it could imply that it is a young star, hence it can have a disk around it which can induce intrinsic polarization. However, all the temperatures found are typical of main sequence stars.

4.1.2 Measurements on the sky

In order to measure polarization we used Stokes parameters q and u. However, the physical quantity which we are interested in is polarization fraction and EVPA. Using equations 3.1 and 3.2 we get p and χ from q and u. We plot the polarization segments for each dp in Fig. 4.2 as they are projected on the sky. Each panel corresponds to a different region. Red lines correspond to the polarization of each star observed and the length of each line is proportional to the degree of polarization. All the angles have been transformed to galactic angles according to [Stephens et al.(2011)]. A segment which indicates the polarization scale of the image appears on the top left of each panel.

Inspecting and comparing all the panels of Fig. 4.2 the argument of qu plane symmetry we employed in the previous section becomes clearer. The top panel corresponds to dp1. The random order of polarization segments of this panel reveal the high symmetric distribution of measurements in dp1. Middle and bottom panels correspond to dp2 and dp3 respectively. As we move to dp3 the order of the segments becomes more evident.

4.2 Assessing the qu symmetry

In dp1 there are 7 measurements located in the first quadrant, 8 in the second, 6 in the third and 3 in the fourth. In dp2 there are 9 measurements in the first, 7 in the second, 0 in the third and 7 in the fourth quadrant. For dp3 the numbers are 10 for the first, 3 for the second, 0 for the third and 8 for the fourth quadrant. To quantity how symmetrically the measurements are distributed around zero we define a symmetry parameter, κ, as the fraction between the number of q, u measurements detected in the quadrant with the least measurements over the number of points detected in the quadrant with the most

measurements. For example if a quadrant is empty $\kappa = 0$ while if all the measurements are isotropically distributed $\kappa = 1$. For dp1 and dp2 $\kappa = 0$ because the third quadrant in each region has no measurements. In dp1 the fourth quadrant has the least points, 3, while the second has the most, 8.

The high symmetry in qu plane measurements of dp1 stars indicate that it could be the result of unpolarized stars (q_{real}, u_{real})=(0,0) measured with some uncertainty. While the apparent anisotropy in dp2 and dp3 seems to come from $(q, u) \neq (0, 0)$ measurements. In order to investigate how probable it is to reproduce the observed symmetries from unpolarized stars we performed Monte Carlo simulations.

The errors in each q_i and u_i measurement follow a Gaussian distribution with deviation $\sigma_{q,i}$ and $\sigma_{u,i}$ respectively; i=1,...,N where N is the number of the observations. Let all stars be unpolarized ($q = 0$ and $u = 0$). We draw random numbers from these zero centered Gaussians with spreads equal to the observational uncertainties and create a sample of M mock ($q_{mock,i}$, $u_{mock,i}$) sets that match the number of stars measured in each region. We compute the parameter κ and then compare its value with the one of the real data. We iterate this process one million times. For dp1 we find κ of mock data is smaller than the observed one with probability 0.432. For dp2 and dp3 this probability is 0.0096 and 0.0095 respectively.

This means that the symmetry in dp1 is consistent with the symmetry produced by mock observations centered at zero. In the other dps the symmetry could not be produced by unpolarized stars with confidence more than 99%.

4.3 Mean polarization computation

In order to measure the mean polarization fraction, $p_{averaged}$ and the mean EVPA, $\chi_{averaged}$, for each dp we computed the weighted mean of the q and u measurements of each region. We obtain two single values $q_{averaged}$ and $u_{averaged}$, for each region, and we apply equations 3.1 and 3.2 to derive $p_{averaged}$ and $\chi_{averaged}$. By doing this sparsely distributed measurements which are not consistent with polarization caused by interstellar clouds have zero contribution to the computed mean polarization. Moreover, most of our measurements have low SNR. Low SNR creates intrinsic bias to every single polarization measurement, p_i, [Vaillancourt(2006)] towards higher values. Hence, if we compute $p_{averaged}$ of each region by measuring the average value of the p_i polarization measurements the $p_{averaged}$ value would be overestimated. For these reasons we obtained $p_{averaged}$ and $\chi_{averaged}$ through $q_{averaged}$ and $u_{averaged}$ for each dp.

In table 4.1 we present the results of the averaged values. The mean polarization in dp1 is 5.25σ away from zero, in dp2 polarization is 2.75σ, while in dp1 it is 1.25σ. Thus, we measured significant polarization in dp3 but not in dp1. Dp2 is the marginal case in which we barely detect significant polarization. However, the 2.75σ distance away from zero cannot be neglected and implies that the faintest stars at this region could be polarized. Previous findings regarding the high symmetry of q, u measurements of dp1 are consistent with the zero mean polarization. As we move from dp2 to dp3 the anisotropy of q, u measurements becomes more prominent. The mean polarization of dp2 is slightly away from zero and justifies the small anisotropy of qu plane, while the higher asymmetry of dp3 measurements agrees with the greater mean polarization value

Table 4.1: Weighted averaged Stokes parameters, p and χ derived from the centroid of q, u of each dp.

	$q_{averaged}(\%)$	$u_{averaged}(\%)$	$p_{averaged}(\%)$	$\chi_{averaged}(^o)$
dp1	0.01 ± 0.04	0.05 ± 0.04	0.05± 0.04	38.34 ± 21.6
dp2	0.09 ± 0.04	0.10 ± 0.04	0.11± 0.04	13.06± 9.73
dp3	0.20 ± 0.04	0.04 ± 0.04	0.21± 0.04	6.22± 5.12

measured in this region.

4.4 $p - A_v$ relation

In Fig. 4.3 the mean polarization is plotted as a function of dust extinction for each dp. Dotted line shows the empirical relation $p = 0.3(\%)A_v$. Extinction values, A_v, for each dp have been computed using the E(B-V) galactic map of [Lenz et al.(2017)]. Extinction is related with color index E(B-V) as follows:

$$\frac{A_v}{E(B-V)} = R(v) \tag{4.1}$$

where $R(v)$ is a parameter correlated with the average size of dust grains. For our Galaxy the typical value is $R_v = 3.1$ [Schultz & Wiemer(1975)]. The values of A_v for dp1, dp2 and dp3 are 0.01953 mag, 0.02232 mag and 0.03658 mag respectively.

Dp1 and dp2 are consistent with the emprical equation 1.1 within 1σ significance, while dp3 is 2.5σ away. Inspecting Fig. 1.2 and Fig. 15 in [Panopoulou et al.(2016)] appear many points which do not follow this relation too. We conclude that maximum polarization is not always constrained by the envelope described by equation 1.1. Though, it is an empirical relation and these inconsistencies are not surprising.

4.5 Polarization segments on HI data

Fig. 4.5 plots the velocity slice of the integrated HI intensity overplotted with the segment of the averaged polarization for each dp. The slice of each region corresponds to the integrated HI intensity over the velocity range $[v_{max} - \Delta v, v_{max} + \Delta v]$, where v_{max} is the velocity at which the HI spectrum shows maximum intensity and Δv has been set equal to $6\frac{km}{s}$. Vertical dotted lines in Fig.4.4 show the v_{max} value of each dp. For dp1, dp2 and dp3 v_{max} is -51.427$\frac{km}{s}$, -8.916$\frac{km}{s}$, -12.781$\frac{km}{s}$ respectively. A polarization segment to indicate the polarization scale of each image is plotted on top left of each panel. Top panel corresponds to dp1, the middle to dp2 and the bottom panel to dp3. Inspecting the images there is no clear correlation of the shape of the dominant clouds and the mean polarization direction.

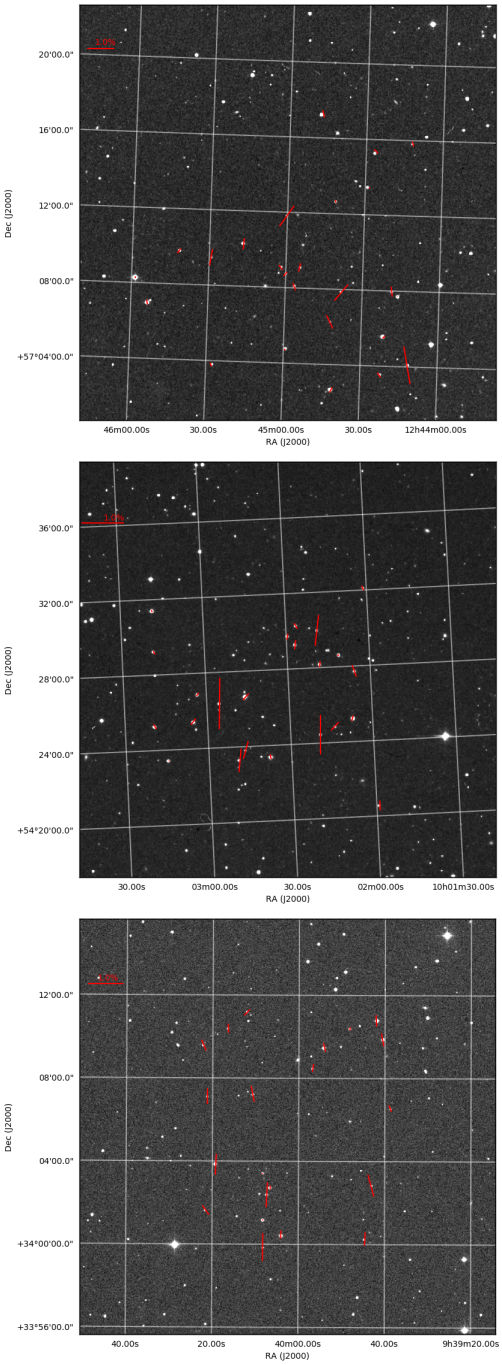

Figure 4.2: Polarization segments over plotted on top of images taken from DSS2-red survey for each region. Each segment's length is proportional to the polarization of the star. A segment on the top left of each panel indicates the scale.

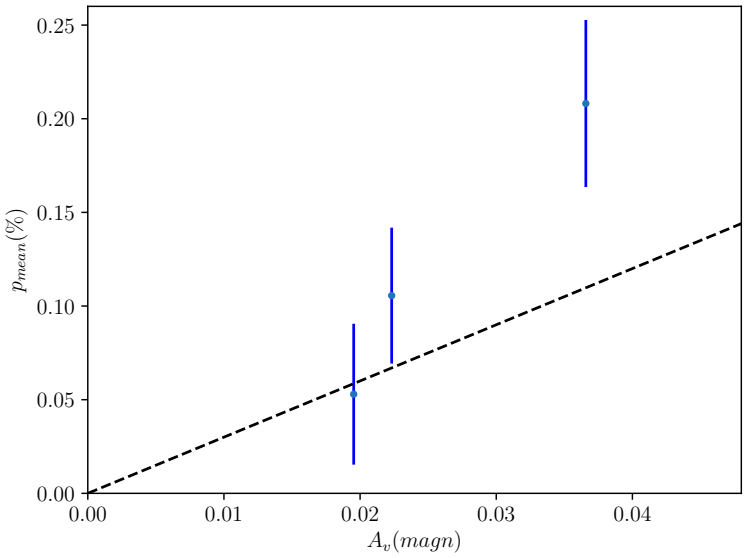

Figure 4.3: Mean polarization, p_{mean}, as a function of dust extinction, A_v for each dp. The dotted black line indicates equation 1.1.

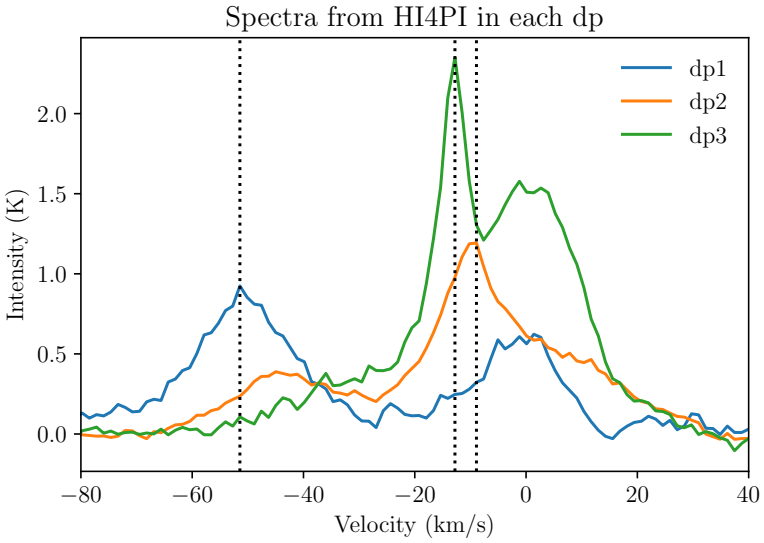

Figure 4.4: HI spectra, intensity as a function of radial velocity, integrated across the line-of-sight of the mean RA and DEC of each dp. Negative velocities indicate gas which is approaching us.

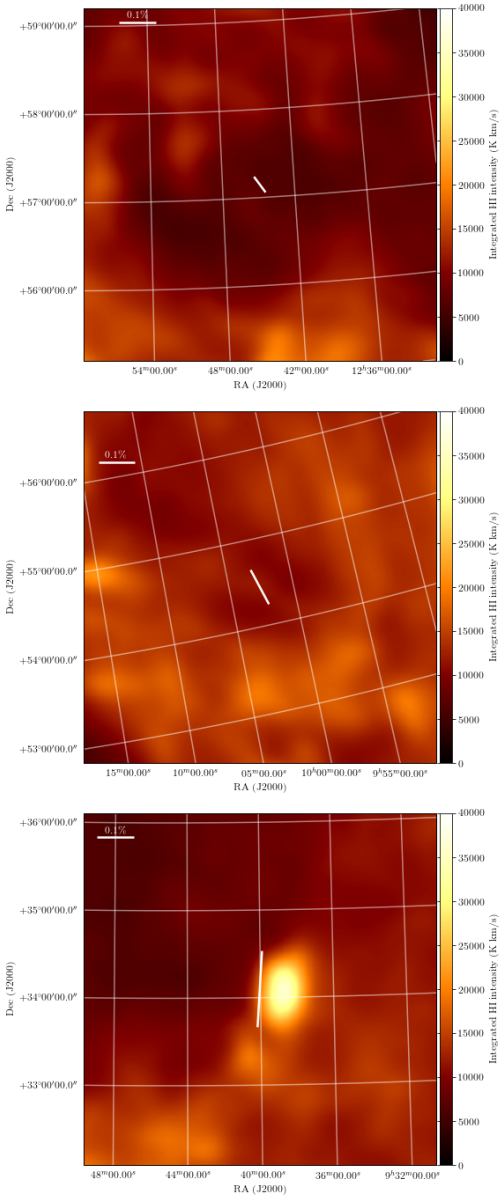

Figure 4.5: Mean polarization direction over plotted on top of images of HI integrated intensity for each dp. Each image corresponds to a velocity channel integrated in a small range, $\Delta v = 6\frac{km}{s}$, about the velocity which shows maximum intensity. A segment appears on the top left of each panel to set the polarization scale. A color-bar is plotted in each panel and shows the intensity levels.

Chapter 5

STOKES PARAMETERS INTRINSIC DISTRIBUTION

The mean Stokes parameter values q_{mean}, u_{mean} have been computed directly from the observations for each dp. In table 5.1 we present the spreads of the q_{obs}, u_{obs} distributions. We do not present dp1 spreads because we could not detect any significant polarization at this region. Because the errors in each individual q, u measurement are comparable to the width of the q_{obs}, u_{obs} distributions respectively the spread values presented in table 5.1 may be not representative of the distribution of intrinsic stellar population. Due to the large observational uncertainties the spread of the real (intrinsic) distribution could be overestimated. In order to estimate what is the spread of the intrinsic distributions of the Stokes parameters we use a bayesian approach.

5.1 Stokes parameters intrinsic distribution spread

Measurements of Stokes parameters have Gaussian uncertainties. This means that if we measure the true (intrinsic) values q_0, u_0 of a star infinite times the distribution of measurements q_{obs}, u_{obs} will be Gaussian with mean values q_0, u_0 and spreads $\sigma_{q,obs}$,

Table 5.1: q_{obs}, u_{obs} distribution spreads for each dp.

	dp2	dp3
$\sigma_{q,obs}(\%)$	0.3130	0.2205
$\sigma_{u,obs}(\%)$	0.1314	0.1187

$\sigma_{u,obs}$ respectively. The probability densities of the measured values q_{obs}, u_{obs} are:

$$p(q_{obs})dq_{obs} = \frac{1}{2\pi\sigma_q^2} exp\Big[- \frac{(q_{obs} - q_0)^2}{2\sigma_{q,obs}^2}\Big] dq_{obs} \tag{5.1}$$

$$p(u_{obs})du_{obs} = \frac{1}{2\pi\sigma_u^2} exp\Big[- \frac{(u_{obs} - u_0)^2}{2\sigma_{u,obs}^2}\Big] du_{obs} \tag{5.2}$$

The joint probability for q_{obs}, u_{obs} is:

$$f(q_{obs}, u_{obs})dq_{obs}du_{obs} = \frac{1}{2\pi\sigma_{q,obs}\sigma_{u,obs}} exp\Big[- \frac{(q_0 - q_{obs})^2}{2\sigma_{q,obs}} - \frac{(u_0 - u_{obs})^2}{2\sigma_{u,obs}}\Big] dq_{obs}du_{obs} \tag{5.3}$$

This equation gives the probability to observe q_{obs}, u_{obs} from a set of intrinsic values q_0, u_0 in the range $[q_{obs}, q_{obs} + dq_{obs}]$ and $[u_{obs}, u_{obs} + du_{obs}]$ respectively.

We assume that the intrinsic values q_0, u_0 are normally distributed about the mean values q_{mean}, u_{mean} with equal spreads $\sigma_{q,0} = \sigma_{u,0} = \sigma_0 = \sigma_{intrinsic}$. The probability then becomes:

$$g(q_{mean}, u_{mean}, \sigma_0)dq_0du_0 = \frac{1}{2\pi\sigma_0} exp\Big[- \frac{(q_0 - q_{mean})^2 + (u_0 - u_{mean})^2}{2\sigma_0^2}\Big] dq_0du_0 \tag{5.4}$$

The spread σ_0 is not the error in the mean value; it is the intrinsic spread in the distribution of the true Stokes parameters around the mean values.

The total probability $F(q_{obs}, u_{obs}|q_0, u_0)$ of measuring q_{obs}, u_{obs} in the ranges $[q_{obs}, q_{obs} + dq_{obs}]$, $[u_{obs}, u_{obs} + du_{obs}]$ and assuming that q_0, u_o follow Gaussian distribution with intrinsic spread σ_0 is given by the product of (5.3) and (5.4). However, in (5.3) it is unlikely to know the intrinsic Stokes parameters, while it is much easier to know the observed values. For this reason we compute the likelihood of measuring q_0, u_0 in the intervals $[q_0, q_0 + dq_0]$, $[u_0, u_0 + du_0]$ with known q_{obs}, u_{obs} .

5.1.1 Maximum likelihood estimation

According to Bayes' theorem for a model characterized by y_i parameters (i.e. q_0, u_0) and measured quantities x_i (i.e. q_{obs}, u_{obs}) we get:

$$P(y_i|x_i) \propto P(x_i|y_i) \tag{5.5}$$

equivalently,

$$F(q_{obs}, u_{obs}|q_0, u_0) \propto L(q_0, u_0|q_{obs}, u_{obs}) \tag{5.6}$$

In words it means that the probability $F(q_{obs}, u_{obs}|q_0, u_0)$ to observe q_{obs}, u_{obs} given q_0, u_0 is proportional to the likelihood $L(q_0, u_0|q_{obs}, u_{obs})$ of measuring q_0, u_0 given q_{obs}, u_{obs}. For a single observation the likelihood is :

$$L(q_0, u_0|q_{obs}, u_{obs})dq_0du_0 = \frac{1}{N} F(q_{obs}, u_{obs}|q_0, u_0)dq_{obs}du_{obs} \tag{5.7}$$

where N is the normalization factor. Integrating over all q_0, u_0 we derive the likelihood function $L(q_0, u_0|q_{obs}, u_{obs})$:

$$L(q_0, u_0|q_{obs}, u_{obs}) = \frac{1}{2\pi\sigma_0^2}\int_{-\infty}^{\infty}\int_{-\infty}^{\infty} dq_0 du_0 f(q_0, u_0)\times \\ exp\Big[-\frac{(q_0 - q_{mean})^2 + (u_0 - u_{mean})^2}{2\sigma_0^2}\Big] \quad (5.8)$$

where $f(q_0, u_0)$ is the joint probability presented in (5.3) with spreads σ_q, σ_u equal to the uncertainty in the observed measurements $\sigma_{q,obs}$, $\sigma_{u,obs}$. The integral in this equation has analytical solution and we present only the result. The analytical proof can be found in appendix of [Venters & Pavlidou(2007)].

$$L = \Big(\prod_{i=1}^{N}\frac{1}{2\pi\sqrt{(\sigma_0^2 + \sigma_{q,obs,i}^2)(\sigma_0^2 + \sigma_{u,obs,i}{}^2)}}\Big)\times \\ exp\Big[-\frac{1}{2}\Big(\sum_{i=1}^{N}\frac{(q_{obs,i} - q_{mean})^2}{\sigma_{q,obs,i}^2 + \sigma_0^2} + \frac{(u_{obs,i} - u_{mean})^2}{\sigma_{u,obs,i}^2 + \sigma_0^2}\Big)\Big] \quad (5.9)$$

All the variables in this function are known except the intrinsic spread σ_0. We compute the likelihood function for various values of σ_0 for dp2, dp3. The spread σ_0 with the largest likelihood value is the best fit for our data. We present the results of this analysis in Fig 5.1. Left panel corresponds to dp2 and the right panel to dp3. The vertical axis shows the likelihood and the horizontal the values of σ_0. Vertical dotted lines pass through the value of σ_0 at which the likelihood peaks. The maximum likelihood for dp2 is $\sigma_0 = 0.0738\%$ while for dp3 it is $\sigma_0 = 0.1453\%$.

5.2 Discussion on the intrinsic spread

Knowing that Stokes parameters are normally distributed we computed the median degree of polarization for both dp2 and dp3 by performing Monte Carlo simulations. We created N (q, u) sets by drawing numbers from Gaussians centered at q_{mean}, u_{mean} with σ_0 spreads. We created a distribution of p values and then we derived the median value of the distribution, p_{median}. The uncertainties in q_{mean}, u_{mean} propagate to the median value. In order to compute them we followed the same process, with which we computed p_{median}, but we drew (q, u) sets from Gaussians centered at $q_{mean} + \delta q$, $u_{mean} + \delta u$ and $q_{mean} - \delta q$, $u_{mean} - \delta u$ respectively. All values, $q_{mean}, u_{mean}, \delta q, \delta u$, are presented in table 4.1. For dp2 $p_{median} = 0.13\%^{+0.05}_{-0.03}$ and for dp3 $p_{median} = 0.26\%^{+0.04}_{-0.03}$.

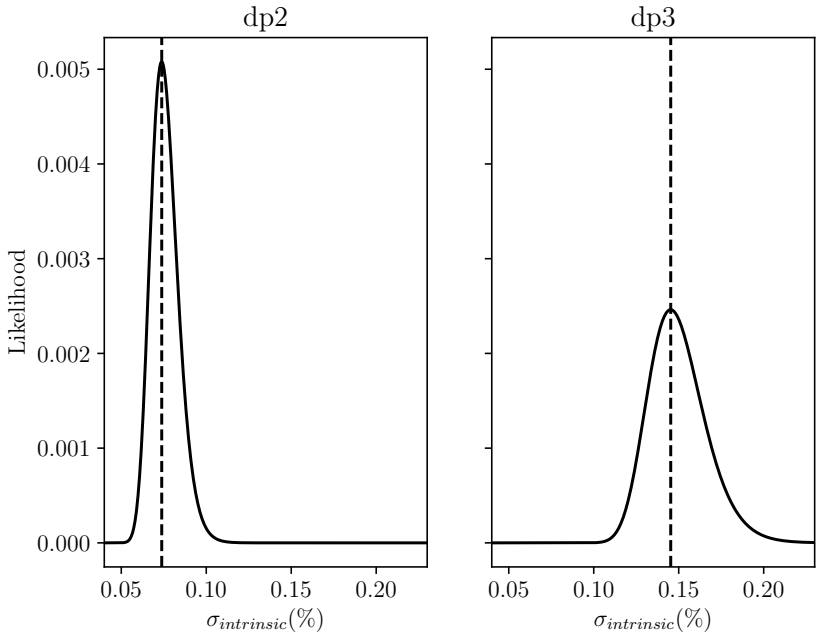

Figure 5.1: Likelihood function for each region. Vertical lines correspond to the intrinsic spread at which likelihood is maximum. For dp1 σ_0 = 0.0738(%) and for dp3 σ_0 = 0.1453(%)

Chapter 6

CONCLUSIONS

In this work we performed three optical polarization surveys at regions, dp1, dp2, dp3 with mean extinction values A_v equal to 0.01953 mag, 0.02232 mag and 0.03658 mag respectively. We explored the previously uninvestigated low extinction regime of the $p - A_v$ relation. Our findings can be summarized as follows:

1. The distribution of q, u measurements on the plane reveal whether the polarization we measure is due to interstellar cloud. In dp1 the high symmetry of the measurements distribution was ascribed to unpolarized stars, while the anisotropy in dp3 measurements is due to a dominant interstellar cloud. Dp2 q, u measurements, on the other hand, despite their high symmetry reveal a slight anisotropy on the qu plane. Dp2 is the marginal case of an interstellar cloud which can barely induce significant starlight polarization.

2. For dp1 we measured $p_{mean} = (0.05 \pm 0.04)\%$, for dp2 $p_{mean} = (0.11 \pm 0.04)\%$ and for dp3 $p_{mean} = (0.21 \pm 0.04)\%$.

3. Measurements of p_{mean} versus A_v for dp1 and dp2 are well correlated with the relation $\frac{p}{A_v} \approx 3\%$, while dp3 p_{mean} is 2.5σ higher.

4. The polarization segment of p_{mean} is not well correlated with the structure of the dominant cloud in any of the regions targeted.

5. The intrinsic spread, σ_0, of the distribution of Stokes parameters for dp2 and dp3 is 0.0738% and 0.1453% respectively.

6. The median polarization fraction, p_{median}, of the distribution of polarization fractions for dp2 and dp3 is $p_{median} = 0.13^{+0.05}_{-0.03}\%$ and $p_{median} = 0.26\%^{+0.04}_{-0.03}$ respectively.

The above suggests that regions with A_v equal to that one of dp2 constitute the threshold above which significant polarization can be detected. With 0.1% accuracy PASHIPAE will not be able to detect significant polarization only for 20.3 square degrees of the sky.

Bibliography

[Andersson et al.(2015)] Andersson B-G., Lazarian A., Vaillancourt J. E.; 2015; ARI; 53:501

[Andersson & Potter(2005)] Andersson, B.-G., & Potter, S. B.; 2005; MNRAS; 356; 1088

[Bayo et al.(2008)] Bayo, A., Rodrigo, C., Barrado Y Navascués, D., et al.; 2008, A& A, 492, 277

[Berdyugin et al.(2001)I] Berdyugin, A., Teerikorpi, P., Haikala, L., et al. 2001, A& A, 372, 276

[Berdyugin et al.(2011)II] Berdyugin, A., Piirola, V., & Teerikorpi, P. 2011, Astronomical Polarimetry 2008: Science from Small to Large Telescopes, 449, 157

[BICEP2] BICEP2/Keck & PLANCK Collaborations: 2015; PRL; 114; 101301

[Chandrasekhar & Fermi(1953)] Chandrasekhar S. & Fermi E.; 1953; Ap. J.; 118:113

[Clemens et al.(2012)] Clemens Dan P., Pinnick A. F., Pavel M. D., Taylor B. W.; 2012; ApJS; 200, 19

[Cudlip et al.(1982)] Cudlip W., Furniss I., King K. J., Jennings R. E.; 1982; MNRAS; 200:1169

[Davis(1951)] Davis L. Jr.; 1951; Phys. Rev.; 81:890

[Davis & Greenstein(1951)] Davis L. Jr., Greenstein. J. L.; 1951; Ap. J.; 114:206

[EBEX] https://arxiv.org/abs/1007.3672

[Eswaraiah et al.(2011)] Eswaraiah C., Pandey A. K., Maheswar, G.; et al. 2011; MNRAS; 411; 1418

[Heiles(2000)] Heiles C.; 2000; AJ.; 119; 923H

[Hiltner(1949)] Hiltner W. A.; 1949I; Ap. J.; 109:471

[Hiltner(1949)II] Hiltner W. A.; 1949II; Science; 109:165

[Hsu & Breger(1982)] Hsu J.-C. & Breger M.; 1982; ApJ; 262; 732

[Inoue et al.(2016)] Inoue Y., Ade P., Akiba Y., Aleman C., Arnold K., Baccigalupi C., Barch B.; et al. 2016

[Kamionkowski et al.(1997)I] Kamionkowski M., Kosowsky A., Stebbins A.; 1997I; Phys. Rev. Lett.; 78:2058

[Kamionkowski et al.(1997)II] Kamionkowski M., Kosowsky A., Stebbins A.; 1997II; Phys. Rev. Lett.; D55:7368

[King et al.(2014)] King O. G., Blinov D., Ramaprakash A. N., Myserlis I., Angelakis E., Baloković M., Feiler R.; et al. 2014; MNRAS; 442; 1706

[Klare et al.(1972)] Klare, G., Neckel, T., & Schnur, G.; 1972; AAPS; 5; 239

[Lenz et al.(2017)] Lenz, D., Hensley, B. S., & Doré, O. 2017, ApJ, 846, 38

[Panopoulou et al.(2016)] Panopoulou G. V.; Tassis K.; Blinov D., Pavlidou V., King O. G., Paleologou E., Ramaprakash A.; et al. 2015; MNRAS; 452; 715

[Papamastorakis(2007)] Papamastorakis Y.; 2007; Ipparchos; 2; 14

[Planck Col.(2013)] PLANCK Collaboration: Abergel A., Ade P. A. R., Aghanim N., Alves M. I. R., Aniano G., Armitage-Caplan C., Arnaud M.; et al. 2014; A& A; 571; A11

[Planck Col.(2016)] PLANCK Collaboration: Adam R., Ade P. A. R., Aghanim N., Arnaud M., Aumont J., Baccigalupi C., Banday A. J.; et al. 2016; A& A; 586; 133

[Rautela et al.(2004)] Rautela B. S., Joshi G. C., Pandey J. C.; 2004; Bulletin of the Astronomical Society of India; 32; 159

[Schmidt et al.(1992)] Schmidt G. D., Elston R. & Lupie O. L.; 1992; AJ; 104; 156

[Schultz & Wiemer(1975)] Schultz, G. V., & Wiemer, W.; 1975; A& A ; 43; 133

[Seljak(1997)] Seljak U.; 1997; Astrophys. J.; 482:6

[Seljak & Zaldarriaga(1997)] Seljak U. & Zaldarriaga M.; 1997; Phys. Rev. Lett.; 78:2054

[Simmons & Stewart(1985)] Simmons J. F. L. & Stewart B. G.; 1985; A& A; 142; 100

[SPIDER] https://arxiv.org/abs/1106.2158

[Stein(1966)] Stein W.; 1966; Ap. J.; 144:318

[Stephens et al.(2011)] Stephens, I. W., Looney, L. W., Dowell, C. D., Vaillancourt, J. E., & Tassis, K.; 2011; ApJ; 728; 99

[Tassis & Pavlidou(2015)] Tassis K. & Pavlidou V.; 2015; MNRAS; 451; 90

[Tassis(2014)] Tassis, K.; 2014; Hipparchos; Volume 2; Issue 2

[Vaillancourt(2006)] Vaillancourt J. E.; 2006; PASP; 118; 1340

[Venters & Pavlidou(2007)] Venters, T. M., & Pavlidou, V.; 2007; ApJ; 666; 128

[Zaldarriaga & Seljak(1997)] Zaldarriaga M. & Seljak U.;1997; Phys. Rev; D55:1830

[Zaldarriaga & Seljak(1998)] Zaldarriaga M. & Seljak U.;1998; Phys. Rev.; D58:023003